Effect of heat treatment and hot isostatic pressing on the structure and mechanical properties of Inconel 939 manufactured via casting and LPBF

Josef Sedlak [a], Jan Zouhar [a,*], Zdenek Pokorny [b], Jan Robl [c], Stepan Kolomy [a], Marek Pagac [d], Karel Kouril [a]

[a] Brno University of Technology, Faculty of Mechanical Engineering, Brno, Czech Republic
[b] Department of Mechanical Engineering, University of Defence in Brno, Brno, Czech Republic
[c] Precision casting division, PBS Velká Bíteš a. s., Velká Bíteš, Czech Republic
[d] Department of Machining, Assembly and Engineering Metrology, Faculty of Mechanical Engineering, Technical University of Ostrava, Czech Republic

ARTICLE INFO

ABSTRACT

The powder bed fusion method is one of the metal additive technologies, which can be used for the fabrication of difficult-to-process materials, such as cobalt and nickel superalloys. Inconel 939 is an example of a nickel superalloy widely used in constructions subjected to high temperatures such as industrial gas turbines. The current paper studies the effect of heat treatment and Hot Isostatic Pressing (HIP) on the structure and mechanical properties of additively manufactured (AM) Inconel 939. Mechanical properties i.e., tensile yield strength, ultimate tensile strength, and creep resistance were observed after the heat treatment (comprised of annealing and subsequent aging), HIP, and compared to the conventionally casted material. HIP post-process caused an increase of 5.73 % and 3.81 % in ultimate tensile strength at the room temperature as well as at the elevated temperature. A detailed analysis of the microstructure of AM and casting samples via light and electron microscopy was performed. The maximum grain sizes in AM samples were similar (122.9 μm and 127.2 μm in the axis and periphery, respectively), while the grain size in casting samples exhibited a mean equivalent circle diameter of 440 μm in the axial region and 398 μm in the vicinity of the peripheral region.

1. Introduction

AM technologies have made a significant progress in recent years, particularly in processing nickel, cobalt, and titanium alloys. The AM process can be divided into three basic steps i.e., pre-processing aimed at preparing a model and the process parameters, processing consists of layer-by-layer deposition, sintering, and solidifying of the actual part [1], and post-processing operation, which involves removing the powder from the building chamber, cutting the models from the building platform and eventually removing supports [2]. AM enables a production of various types of materials, such as 316 L stainless steels [3,4], 15-5PH [5], Inconels [6], Ti alloys [7] or maraging steels [8], whose structures and mechanical properties can be influenced by the used powder [9], process parameters [10], strategies or applied post-processing operations (heat or chemical heat treatment, applying of special coating [11], hot rotary swaging [12], HIP [13], LSP [14], laser polishing [15] topological optimization [16,17] and machining [18] [19])and so on [20].

Inconel 939 is a nickel-based superalloy with remarkable material properties for extreme conditions, in which these alloys can operate as high-pressure turbines [21]. Inconel 939 is very used in the aerospace industry due to its high-temperature corrosion, oxidation resistance, and creep strength [22]. These superalloys are used in more than 50 % of components (liquid-fuel rocket engines, satellite components, turbomachinery, propellant tanks, and others [23]) of aerospace engines [24,25].

But what is the benefit of superalloys in terms of their mechanical properties is a disadvantage in terms of their machinability, such as their toughness, hardness, high-temperature resistance, creep resistance, etc. [26]. Therefore, AM has become a more and more popular technology for production of industrial components (manufacturing tools, forms, or small series components) from superalloys [27,28]. However, AM requires a further research on the final Inconel 939 microstructure and its impact on the mechanical properties and how they differ from conventional processing methods [29].

Creep properties, which depend on AM technology and heat

* Corresponding author.
E-mail address: zouhar@fme.vutbr.cz (J. Zouhar).

Table 1
Chemical composition of a virgin powder used for the sample fabrication.

Element	Cr	Co	Al	Ti	W	Mn	Nb	Ta	Ni
(Wt%)	22–23	18–20	1–3	3–4.5	1–3	0.04	0.5–1.5	1–1.8	Balance
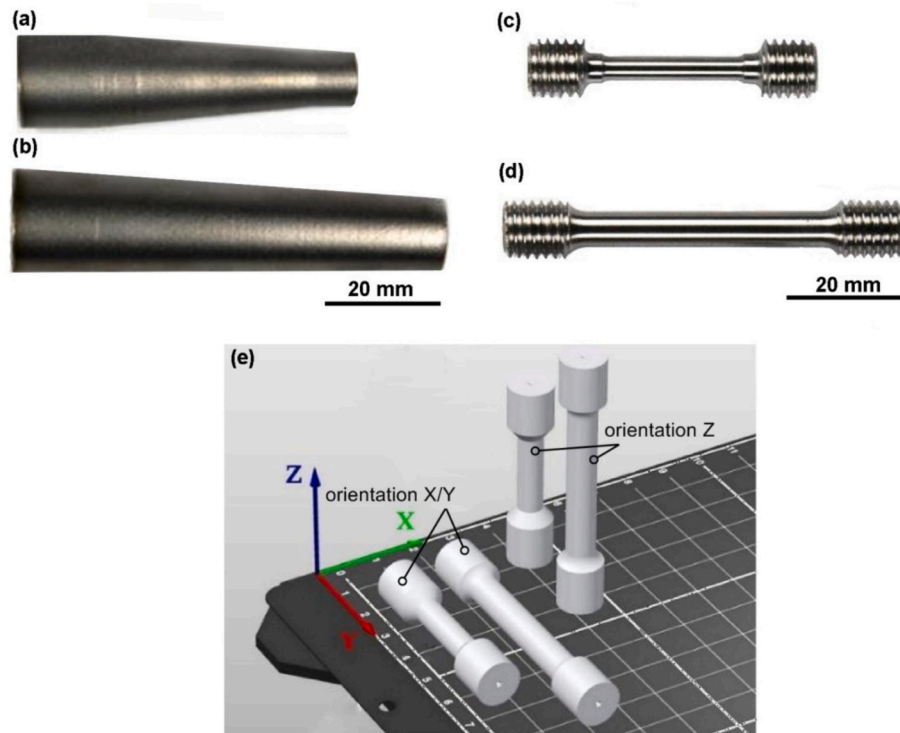
Fig. 1. (a) precision cast blank used for the creep resistance test, (b) precision cast blank used for the tensile test, (c) prepared sample used for creep resistance test, (d) prepared sample used for tensile test and (e) types of sample orientation when 3D printing used for further analysis.

treatment conditions were studied by Banoth et al. [30], who discovered that a lower temperature during the heat treatment was not sufficient for AM Inconel 939, because it exhibited a lower creep life compared to the cast specimen. Because the life of high-temperature alloys is highly influenced by their creep resistance, it is important to understand the various microstructural parameters such as used materials and other factors controlling their creep resistance [31].

AM Inconel 939 has been the subject of many research studies in recent years, which tried to monitor its behaviour under different conditions. As mentioned above, the final properties of AM Inconel 939 are affected by many factors attributed to the building cycle and its process parameters, powder mixture, or environment [32]. Regarding powder material properties, powders with fine sieving fractions are more suitable for the fabrication of dimensionally more accurate and smooth surfaces. On the other hand, their flow rate is worse, and it is more difficult to dispense them [33]. Interesting findings are also brought by Tang et al. [34], who discovered that superalloys, which were not designed for AM did not feature a suitable composition and there are possibilities for future research to improve their composition to increase mechanical properties. Therefore, results obtained in the current study about Inconel 939 can support future research in this field. Regarding process parameters, Marchese et al. [35] discovered that the most appropriate hatch distance of AM Inconel 939 was 0.03 mm because it provided a sufficient overlap between consecutive laser scans which imparted a reduction of cracking density and residual porosity.

Ozaner et al. [36] studied the effect of creep feed grinding and wire electrical discharge machining methods on the surface integrity of AM turbine blades of gas turbines. They found out that the electrical discharge machining method brought about more favourable results

regarding the mechanical properties. Another frequently studied post-processing operation is welding, especially the influence of process parameters on crack formation. Generally, as more studies showed, Inconel 939 can be welded with the satisfying weld quality. The most common problem during welding is cracking, which depends on the type of welding, welding speed, heat input or energy per unit length, type of filler alloy, microstructure of welded material, hardness, and other parameters [37,38,39]. González Albarrán et al. [40] pointed out that pre-weld heat treatment could improve the weldability of Inconel 939, which exhibited a decrease in cracking in the heat-affected zone.

Heat treatment is an effective way to improve the mechanical properties of Inconel 939, due to a dissolution of the dendritic microstructure and precipitation of the γ' precipitates in the microstructure [41]. The heat treatment increases the volume fraction of these precipitates as well as the yield and ultimate tensile strength [42,43]. For example, the tensile strength was increased by heat treatment applied by Gusain et al. [44]. In addition, Jahangiri [45] found out that the γ' precipitates can increase the hardness of Inconel 939 superalloy more when they have nanoscale dimensions. Especially in the aerospace industry, the microstructure stability under prolonged thermal exposures is critical [46]. The heat treatment can ensure this stability, but there is still not enough knowledge in this field, and the further research is required. Besides the microstructure of Inconel 939 can be improved by other types of treatments. For example, Shaikh et al. [47] studied the suitability of the AM Inconel 939 microstructure for aging with and without a solution treatment. Their results showed that the solution treatment is probably not necessary for the dissolution of the γ' phase, but it is critical for removing the η phase from the microstructure. On the other hand γ' phase precipitated within the matrix after all solution heat
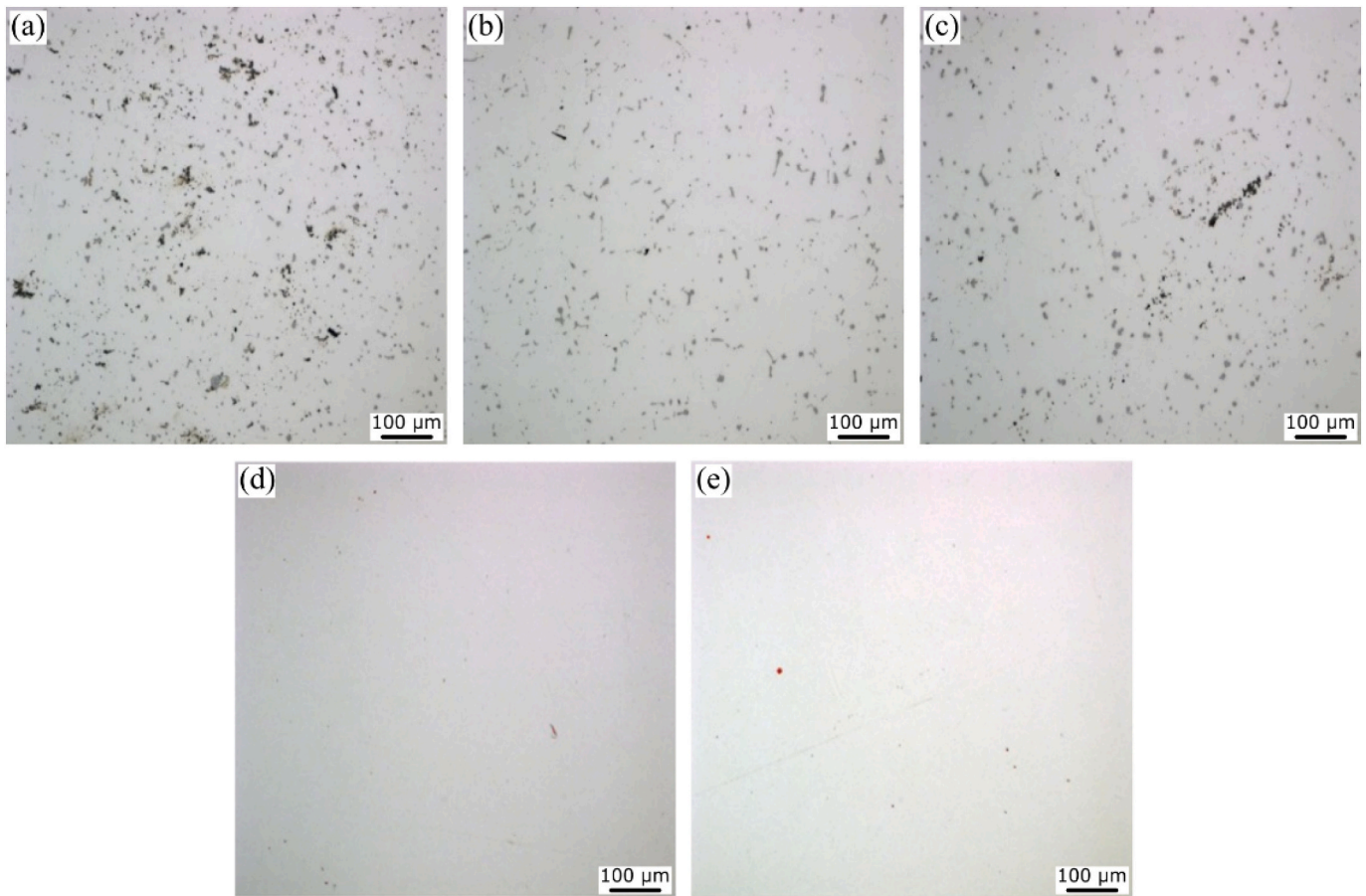
Fig. 2. Light optical microscopy (LOM) images show porosity (cross-section in middle height) in (a) cast sample, (b) cast and HT sample, (c) cast and HIP sample, (d) sample with layer thickness of 30 μm and post-processed by HT and (e) sample with layer thickness 60 μm and post-processed by HIP.

Table 2
Sample porosity evaluated after different post-processing operations.

Sample	(A)	(B)	(C)	(D)	(E)
Type of production	Cast	Cast (HT-C)	Cast plus HIP (HIP-C)	AM (30 μm, HT-P)	AM (60 μm, HIP-P)
Porosity (%)	0.400	0.100	0.120	0.004	0.012

treatment conditions, which led to increase in the microhardness values as observed by Doğu et al. [48].

Due to the shortage or even nonexistence of studies focused on effects of HIP and heat treatment on creep properties of Inconel 939 manufactured via PBF, this study was conducted., Detailed analysis of the mechanical properties and microstructure of AM and casted Inconel 939 materials post-processed by the heat treatment and HIP were performed to fill the research gap. The novelty of this paper is the examination of HIP post-process operation on the microstructure and mechanical properties i.e., ultimate tensile strength (UTS), yield strength (YS), and creep resistance of Inconel 939. The thorough microstructure analysis i. e., porosity evaluation via light optical microscopy, SEM, TEM, and EBSD were performed. In addition, a detailed fractographic analysis was used to observe fracture surfaces. The results were compared with the conventionally casted material and the differences between the microstructure and mechanical properties of tested samples were evaluated. The main purpose of this study was to investigate the possibility of using AM to produce a turbine engine axial impeller from the relatively new material Inconel 939.

2. Experimental procedure

2.1. Sample preparation

Samples from the Inconel 939 powder mixture were 3D printed and casted via precision casting. The chemical composition of the material is given in Table 1. Tensile tests were carried out according to EN ISO 6892-1 (under room temperature) and ISO EN 6892–2 (at an elevated temperature) and for the creep strength test according to EN ISO 204. Raw material for the test samples prepared by casting for both tests (at room and elevated temperature) are shown in Fig. 1a and b. Fig. 1c and d show machined samples used for testing. The technology of precision casting into a water-based ceramic malachite shell was used to produce casting samples. The final composition of the metal came from a virgin material directly from the supplier. AM specimens for tensile and creep tests were manufactured on the 3D printer (SLM 280 2.0, SLM Solutions Group AG) using a powder mixture in the range of 10–45 μm. The entire building cycle took place on the mentioned device with process parameters recommended by the powder supplier of the Inconel 939 material. In particular laser power was set in range 27–370 W (depends on the printing zone), scanning speed was set in range 500–7000 mm.s^{-1}, hatching distance was determined in range 0.06–0.11 mm. The 3D printed samples exhibited a 1.2 mm allowance on their diameter. This allowance was removed by finishing operation using a cutting insert with 0.4 mm nose radius. All 3D printed samples were marked according to their orientation during 3D printing (see Fig. 1e). The samples 3D printed parallel to the z-axis were indicated as Z orientation. Also, the samples 3D printed perpendicularly to the z–axis were indicated as X/Y orientation. The layer thickness was chosen as either 30 or 60 μm, which
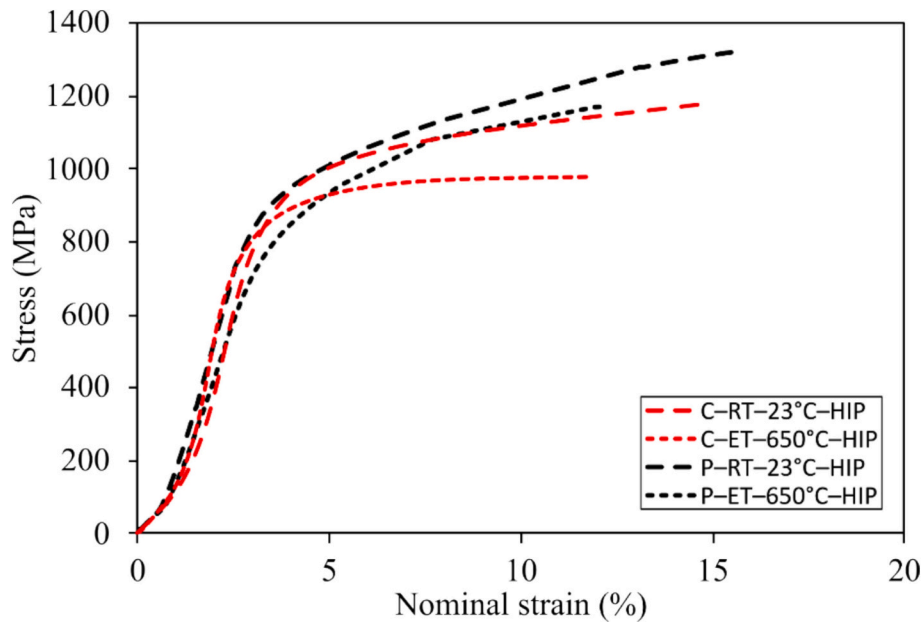
Fig. 3. Dependence of stress on nominal strain for the printed and casted samples under RT and ET.

was further marked for each sample.

2.2. Post-processing operation

The process of the heat treatment depends on the technology of the production of semi-finished products. The procedure of the heat treatment (prescribed by the powder supplier) was followed for the casted as well as for the 3D printed samples. The HIP operation was also included in the heat treatment of few samples, which combining the temperature of up to 2000 °C with a pressure of up to 2070 bar leads to the elimination of pores in the material and conversion of some undesirable structures, such as oxides, nitrides and some forms of carbides [49]. The annealing heat treatment was performed by rapid heating (RH) to 1107 °C/2 h in a vacuum furnace followed by a slow cooling (3 °C/min) to 899 °C. After reaching a temperature of 899 °C a rapid cooling (RC) with Ar to the room temperature (RT) was carried out. Subsequent aging consisted of three steps i.e., RH to 913 °C/8 h plus RC with Ar at RT, RH to 982 °C/6 h plus RC with Ar at RT, RH to 803 °C/4 h, and quenching with Ar to RT. The HIP post-process operation was realized as a combination of the identical heat treatment with HIP at the temperature of 1200 °C/4 h and the pressure of 1000 bar.

The casted samples were heat treated with homogenization annealing followed by aging. Homogenization annealing was carried out at the temperature of 1160 °C/2 h followed by cooling (30 °C) to the temperature of 700 °C followed by the air cooling to RT. The aging treatment was carried out at the temperature of 845 °C/16 h with fan cooling to RT. Few samples were subjected to the HIP process parameters at a temperature of 1200 °C/4 h and the pressure of 1035 bar in Ar atmosphere with a minimum purity of 99.995 %.

For a better recognition and simpler orientation among individual samples, a clear identification system was developed. The first character was assigned to the production technology: P for the 3D printed samples and C for the casted samples. The second dashed character indicates the type of test being performed: RT for tensile tests at room temperature, ET for the tensile tests at elevated temperatures, and CR for the samples designed for the creep resistance tests. In the case of tests of the 3D printed material, information about the build orientation (Z or X/Y) and layer thickness (30 or 60 μm) was also added. The following designations were chosen for the type of heat treatment i.e., heat treatment of the casted samples (C–HT), heat treatment of the 3D printed samples

(P–HT), heat treatment + HIP of the cast samples (C–HIP), heat treatment + HIP of the 3D printed samples (P–HIP). To obtain relevant results five samples were tested for each variant mention above. All samples intended for testing were places randomly on the building platform to avoid any accidental anomalies caused by 3D printing process.

2.3. Mechanical properties and structure observation

The tensile tests at RT were performed using the TIRAtest 28,250 machine (TIRA GmbH). The creep resistance tests were carried out via a T-800 machine (SVUM GmbH). The limit condition for testing under the temperature of 870 °C and a load of 255 MPa was set to 60 h of break time with a minimum elongation of 5 %. For the test at 982 °C and 112 MPa, the minimum fracture time was set at 40 h with a minimum elongation of 5 %. The study of the fracture surfaces and microstructure was performed using a Lyra 3 scanning electron microscope (SEM, TESCAN, Brno) equipped with an energy-dispersive X-ray detector (EDX). A microstructure was observed after a metallographic preparation via conventional techniques such as grinding, polishing with diamond pastes, and etching. After etching (2 g $CuCl_2$ + 40 ml HCl + 40 ml ethanol) for 10 s, the samples were observed via SEM (the backscattered electron detector was used in all cases) and light microscopy using Axio observer Z1m from ZEISS.

Scanning electron microscopy (SEM) was used to perform electron backscatter diffraction (EBSD) analyses of the cast and 3D-printed materials subjected to HIP. The analyses were carried out using a Tescan Lyra 3 XMU FEG/SEMxFIB microscope equipped with a Symmetry EBSD detector (Tescan Orsay Holding a.s., Brno, Czech Republic). Cross-sectional cut of the samples from both materials were mechanically ground via SiC papers and then electropolished. Scanning was performed with 70° tilted samples. EBSD scans from the 3D printed material were carried out on an area of 300 × 500 μm with a scan step of 0.5 μm, whereas the scans acquired from the casted material had an area of 2500 × 2000 μm and the scan step of 5 μm. During evaluations of the scanned data, the limiting value for low angle grain boundaries (LAGB) was 5°, while for high angle grain boundaries (HAGB) it was 15°. The lamella was produced using a Helios-type electron microscope from THERMO FISHER, which was also equipped with a focused intense beam (FIB). This lamella was intended for the study of material composition
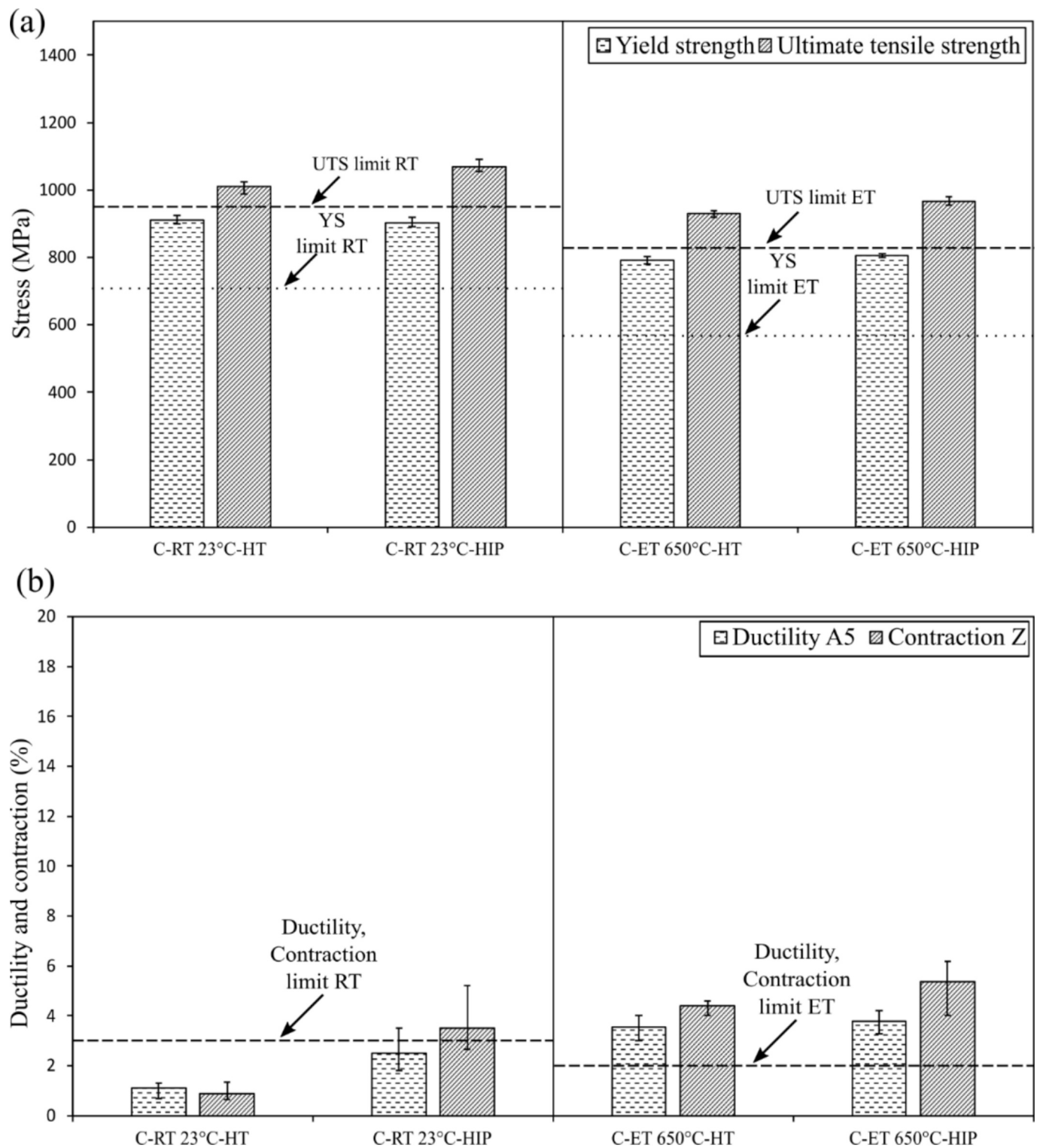
Fig. 4. (a) Outputs of the tensile test at the RT and ET for the individual cast samples, while the limit of YS and UTS are indicated by the pointed and dashed lines, and (b) the outputs of the tensile test, while the limit for ductility A5 and contraction Z are marked with the same interrupted lines.

using EDX in a transmission electron microscope (TEM) of the Titan type from THERMO FISHER.

3. Results and discussions

3.1. Porosity evaluation

The AM technology such as powder bed fusion can manufacture a microstructure with minimal porosity [50]. Set process parameters can change the forming of the structure, especially the final porosity
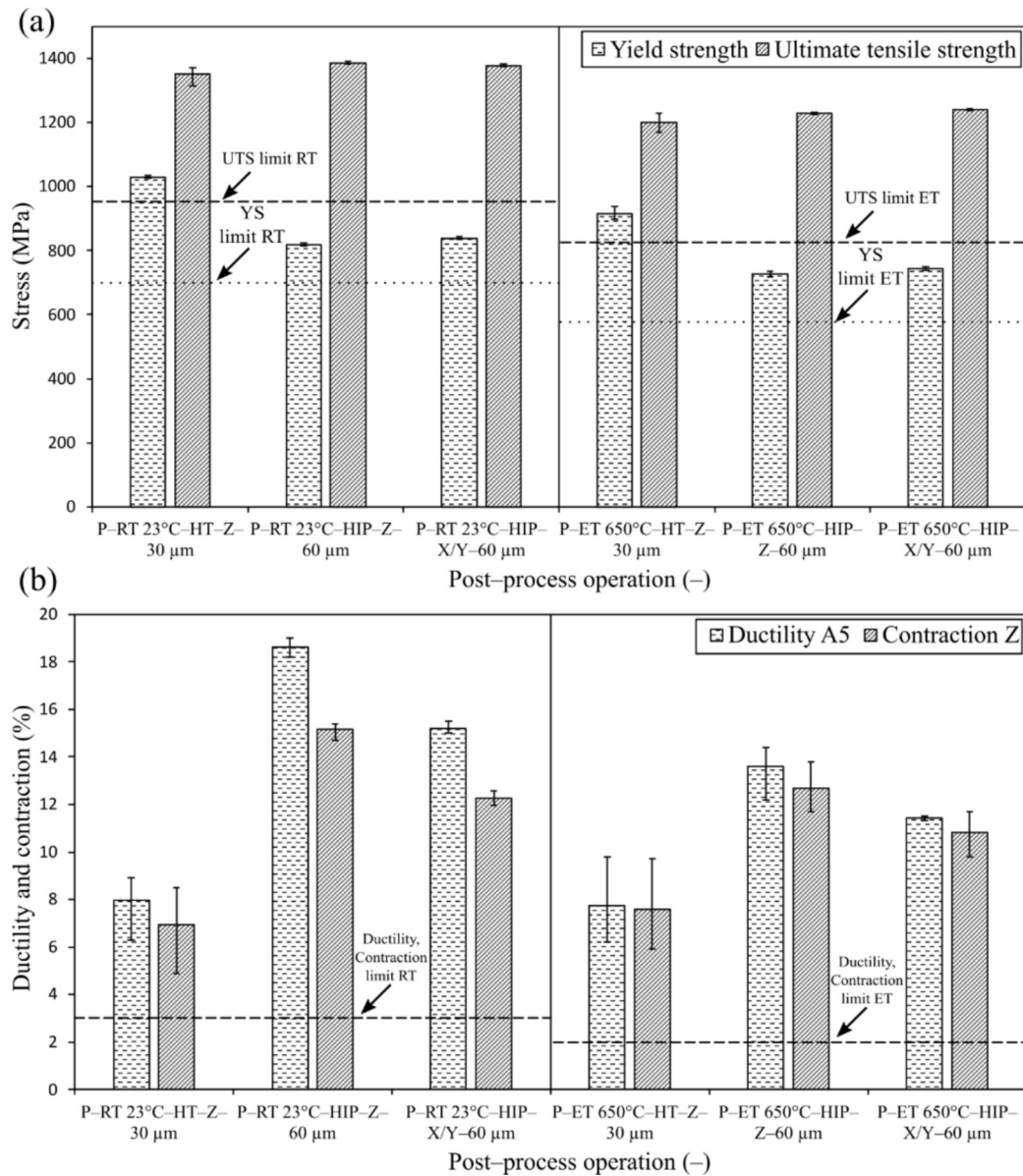
Fig. 5. (a) Outputs of the tensile tests at RT and ET for individual 3D printed samples, while the limit of YS and UTS are indicated by the dashed and interrupted lines, and (b) the outputs of the tensile test, while the limit for ductility A5 and contraction Z are marked with the same interrupted lines.

[51,52], which includes pores, cavities, or voids occurring within the structure due to the protecting gas entrapped in the material during the building process [53,54]. Structure, which features lower porosity will perform higher fatigue resistance and mechanical properties [55]. The porosity was evaluated on the light images (see Fig. 2a-e) via the software AxioVision in the middle height of the sample due to the expectance of the highest porosity in this location. The light image with the highest observed porosity was chosen for the further evaluation. The obtained results are listed in Table 2. It can be seen that sample A exhibited the highest observed porosity in the as-casted state. After the heat treatment, the porosity was reduced as can be seen in samples B and C. A small difference was evaluated among samples B and C even after HIP a slight increase was observed (depending on the measured place). AM samples featured the lower porosity in comparison to the casted samples. Sample D exhibited a lower porosity compared to sample E due to the lower layer thickness, which can reduce a few pores and voids [56].

3.2. Tensile test

Fig. 3 shows a graph depicting the dependence of stress on nominal strain for the 3D printed and casted samples tested under RT and ET. The course of the stress is typical (neither an upper nor a lower yield stress point was seen) for a material with high toughness. It can be seen that the strain hardening is lower at ET as well as the elongation. The absorbed energy is higher in the case of testing under RT in comparison to the ET. Hence a fraction point in P–RT– HIP occurred under higher stress than in P–ET– HIP. Each sample featured a similar course with different values of YS and UTS.

The UTS limit and the YS limit were chosen as the initial criteria for the evaluation of the tensile test results under RT as well as EL, which is visualized by pointed and dashed lines depicted in Figs. 4a and b. The YS is one of the initial criteria, which is used for components design in heat-resistant applications. The UTS limit and YS limit were reached by all casted samples. The inclusion of the HIP operation in the heat treatment of casted Inconel 939 resulted in a slight increase in the UTS. In other words, the HIP operation yielded higher mechanical properties (an
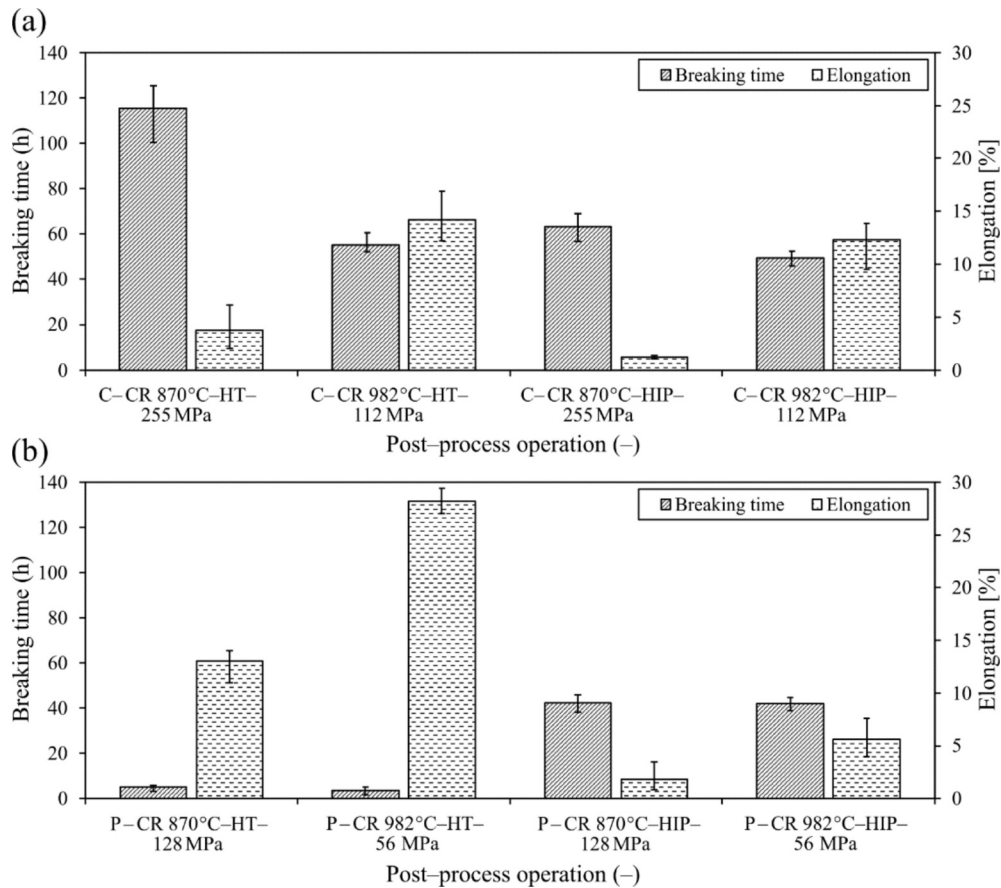
Fig. 6. Outputs of the CR tests for the cast and 3D printed samples post-processed by HT and HIP, (a) the graph represents breaking time and elongation for the C–HT and C–HIP samples tested under the temperature of 870 °C and 982 °C and load 255 MPa and 112 MPa, respectively and (b) characterization of the P–HT and P–HIP samples tested under the temperature of 870 °C and 982 °C and load 128 MPa and 56 MPa, respectively.

increase of 5.7 % in UTS). The casted samples post-processed by the heat treatment did not reach the ductility A5 at RT. By including the HIP operation in the heat treatment, it was possible to observe an improvement in the ductility and contraction of the material, however, only the contraction reached the prescribed limit at RT. The same trend (an increase of 3.9 % in UTS after HIP) was observed in the case of tensing under ET. The ductility limit of the casted samples at ET of 650 °C complied with the requirements for all tested samples. During the test, the HIP featured none significant effect on the resulting ductility of the casted material, but the contraction Z showed an increase after the HIP. The initial criterion for the evaluation of the tensile test results under the ET of 650 °C was the limit of the minimum YS given according to the lowest possible value, which can be used as a propeller in the high-temperature environment.

Fig. 5 shows the results for the 3D printed samples obtained for different types of testing. The highest observed YS was obtained in the case of the samples, which were built with the 30 μm layer thickness (see Fig. 5a). It was an increase of 25.8 % and 22.6 %, respectively in comparison to the samples with the 60 μm layer thickness and post-processed by the HIP. It can be stated that not only the layer thickness but also a build orientation (Z, X/Y) affected the final mechanical properties. In regards to the UTS the samples heat treated and HIPed exhibited a higher value compared to the samples without HIP. A very similar trend was observed under ET, where the highest UTS was reached for the samples fabricated with 60 μm layer thickness. Nevertheless, all 3D printed samples complied with the limit of the YS and UTS (visualized in each figure) under RT and ET. A significant improvement of the ductility A5 was observed in the 3D printed samples at RT compared to the P–RT–HT samples, which increased (by 10.6 % for the Z

orientation and 7.2 % for the X/Y orientation on average, respectively) not only due to the higher layer thickness but also due to the HIP operation, which was included. The similar trend was obtained for the 3D printed samples tested at ET, where the highest ductility A5 and contraction Z were approached in the samples 3D printed in Z orientation. In comparison to the P–ET–HT samples the P–ET–HIP samples reached the higher ductility A5 (an increase of 5.9 % for the Z orientation and 3.7 % for the X/Y orientation on average, respectively) and contraction Z (the similar trend was observed). In other words, it can be stated that all 3D printed samples met the prescribed limits of ductility A5 and contraction Z (see Fig. 5b).

Since the Inconel 939 material in 3D printed form has not yet been tested under RT and ET in other studies by a tensile test, a comparison was performed with other types of Inconel e.g., testing of the printed Inconel 718 brought the UTS of 1287 MPa [57], which is a lower compared to values obtained in the current study. Nguyen et al. [58] reached similar values (as achieved in the current study for Inconel 939) of UTS and ductility A5 for 3D printed Inconel 718. The higher layer thickness (60 μm) resulted in higher observed ductility compared to the sample produced with the layer thickness of 30 μm. It can be concluded that the HIP post-process positively influenced final mechanical properties.

The casted material exhibited a lower value of UTS as well as the lower ductility A5 in the case of all samples in comparison to the 3D printed samples, but contrary in regards of the YS the quite opposite trend was observed. This phenomenon was shown very likely due to the higher porosity (defined in section 3.1) and different structure (describe in detail in the section 3.3). Considering the ductility A5 and contraction Z a higher difference was obtained, where the 3D printed samples
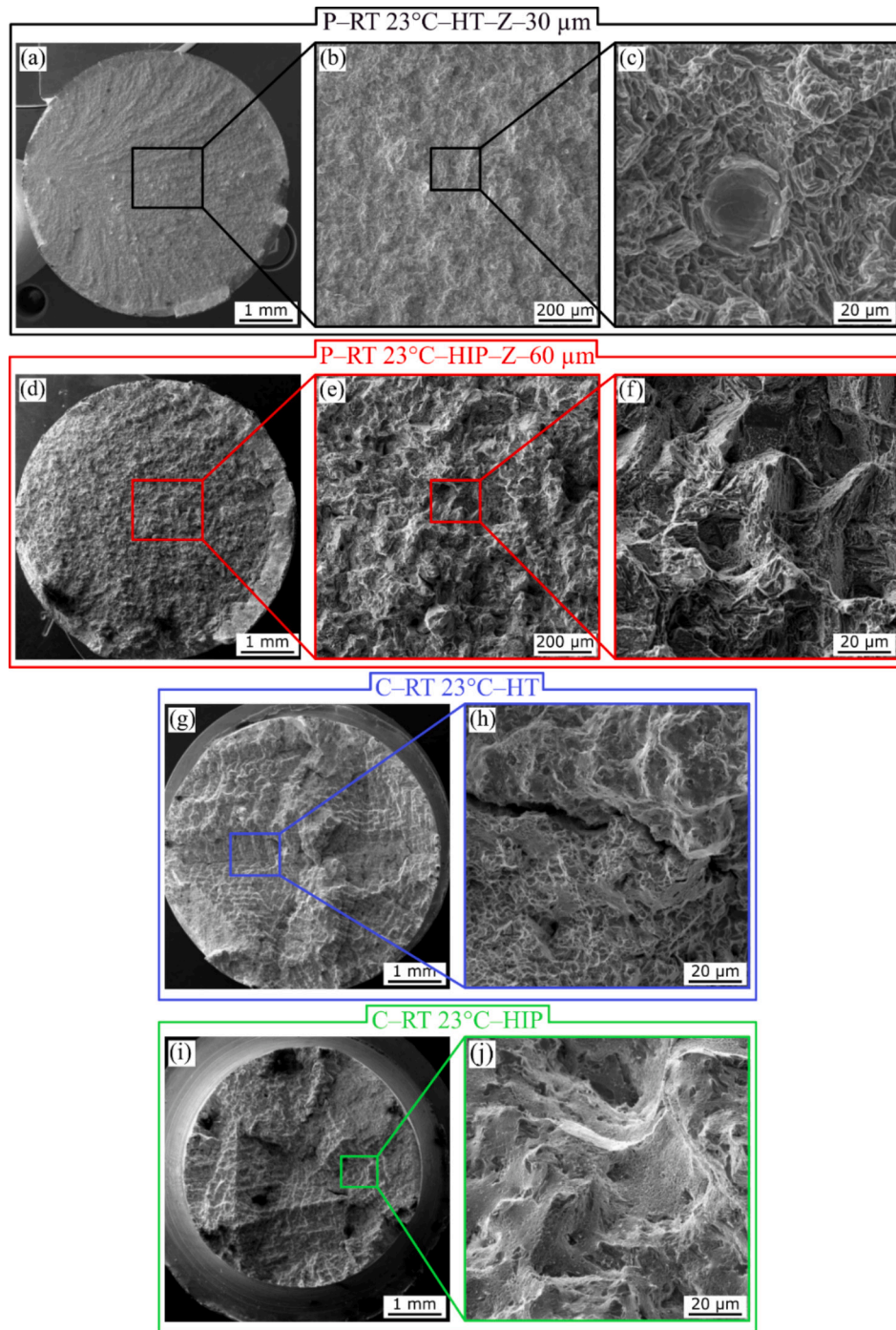
Fig. 7. SEM images of the sample P–RT–HT with the layer thickness of 30 μm (a-c), the P–RT–HIP sample with the layer thickness of 60 μm (d-f), the C–RT–HT sample (g and h), and (i and j) the C–RT–HIP sample.

featured a higher value at RT as well as at ET compared to the cast samples.

3.3. Creep test

The results of the casted samples used for the creep testing are depicted in Fig. 6a. The specimens subjected to the creep test at 870 °C featured the higher breaking time in comparison to the samples tested under 982 °C. But contrary the course of the elongation exhibited an opposite evolution. The difference reached 60.4 h and 10.4 % respectively. The similar trend was seen in the case of the samples post-processed by the HIP, but the difference in results were lower than in

case of HT samples. From global point of view the HIPed samples resulted with lower breaking time and elongation. Furthermore, based on the obtained results a significant influence of the post-process (HT, HIP) on the final breaking time and ductility of the samples was observed. However, the samples with the included HIP operation achieved the lower breaking time as well ductility. It can be explained by the lower average grain size (reduced by applied HIP [59]), which was not suitable for the creep resistance [60].

A few of 3D printed samples for the layer thickness of 30 μm and 60 μm were chosen for the creep tests. Unfortunately, the results showed poor results for both types of samples. Hence the applied stress was reduced in the following tests to 50 % of the original stress. Finally, the
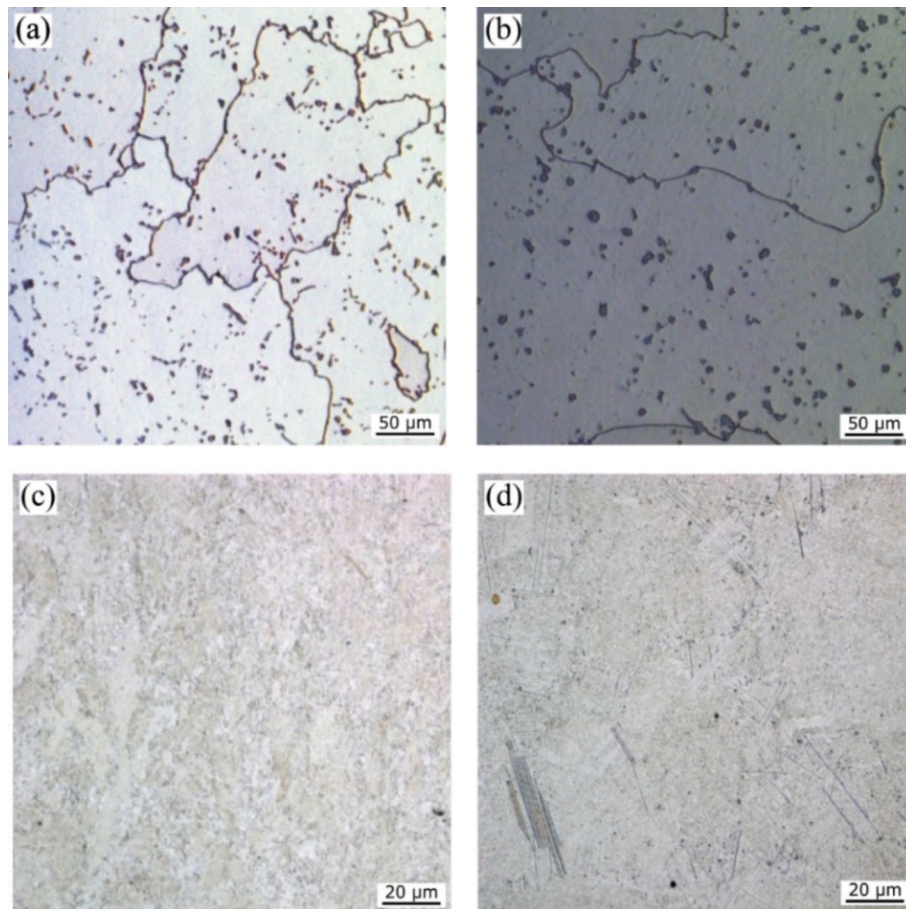
Fig. 8. Light optical microscopy (LOM) images of the C–HT (a), the C–HIP sample (b), the P–HT sample with the layer thickness 30 μm (c), and (d) the P–HIP sample with the layer thickness 60 μm.

stresses 128 MPa at the temperature of 870 °C and 56 MPa at 982 °C were used respectively. Regarding the P–HT samples, the breaking time was significantly lower than in the case of the P–HIP samples, but the elongation featured the higher values respectively (see Fig. 6b). The creep tests were performed on the samples fabricated with the 60 μm layer thickness because the samples with the 30 μm layer thickness achieved poor breaking time. Hence the higher breaking time was expected due to the higher layer thickness causing the larger grain size, which can impart more favourable CR and HIP post-process reduces initial impurities such as pores voids, etc. [61]. The lower CR of the 3D printed samples compared to the casted ones can be explained by the lower average grain size (Lee et al. found out that an initial strain at the beginning of creep tests decreased with the decrease of grain size), which resulted in the poorer creep resistance [62]. However, the P–HIP samples resulted in a higher breaking time than the P–HT samples. It can be concluded that HIP had a positive effect on the final CR. The creep test results of Inconel 939 have not been yet presented in other studies, therefore a comparison with other studies is not possible. The CR of Inconel 718 reached similar or slightly lower values compared to the results obtained in this study [63,64,65]. However, the 3D printed Inconel 625 featured lower CR in the study presented by Leary et al. [66].

3.4. Fractographic analysis of fracture surfaces

The analysis of fracture surfaces (see Fig. 7) was carried out on the selected samples tested under RT using SEM. These samples, which were selected exhibited the lowest UTS. Specifically, the samples P–RT–HT with the 30 μm layer thickness, P–RT–HIP with the 60 μm layer

thickness, C–RT–HT, and C–RT–HIP. The morphology of the 3D printed material showed signs of ductile fractures. In the P–RT–HT sample, the initiation of the fracture (see Fig. 7a) on the surface with a gradual propagation of the formed crack was evident. After a more detailed sample examination, further scanning was focused on the defects of the P–RT–HT sample captured in Fig. 7b and c, where a more detailed imaging of the spherical cavity took place. Similar spherical cavities were also observed on the Inconel 718 samples with layer thicknesses of 30 and 50 μm [67] and also in the Pradeep study [68]. The spherical cavity was determined as an imprint of an unmelted metal powder particle that remained trapped inside the material during the building process and was released from the material after a tensile test. Validity of this conclusion is also confirmed by the shell morphology of crack propagation in the entire cross-section of the sample. The fracture surface of the 3D printed sample P–RT–HIP (see Fig. 7d-f) is very similar to the fracture surface in the McLouth [69] or Wang [70] study for Inconel 718. In the examined sample C–RT–HT seen in Fig. 7g and h was possible to observe the remains of secondary cracks formed at the grain boundaries, which emerged into the fracture surface of the main crack during the tensile test. The sample post-processed by HIP (C–RT–HIP) technology showed signs of ductile fracture. The facets protruding into the fracture surface of this sample indicate the propagation of cracks along the dendrites and grain boundaries.

3.5. Structure observation

Fig. 8 shows light optical microscopy images taken from the casted and as-built samples. The images represent the transverse cross-section (perpendicular to the building direction) in case of Z oriented samples.
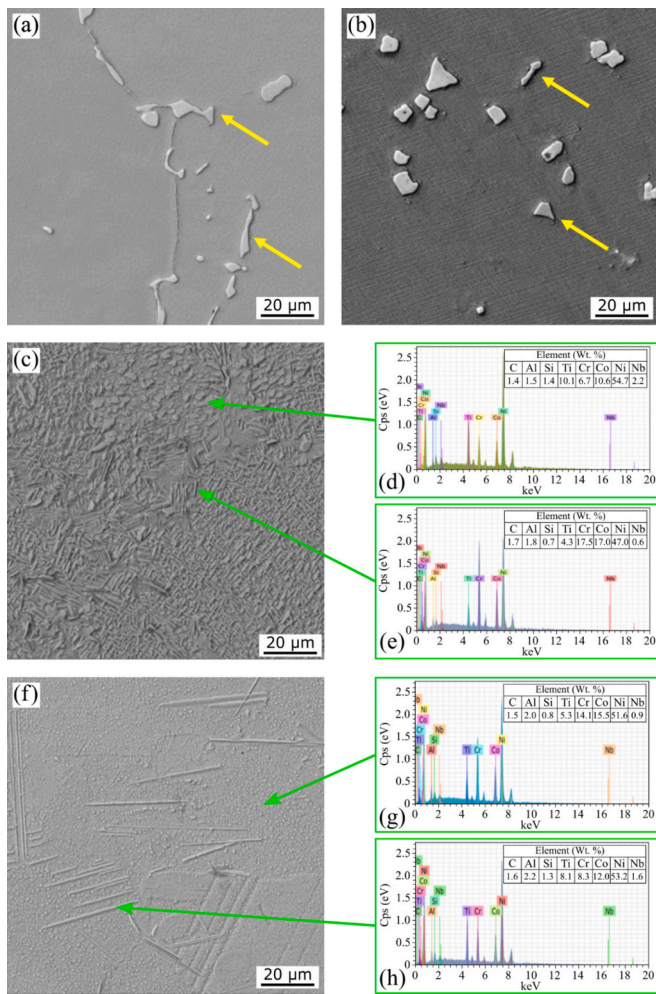
Fig. 9. SEM images of the C–HT with excluded MC carbides (a), the C–HIP sample with excluded MC carbides (b), the P–HT sample with a layer thickness 30 µm (c), EDX analysis of the P–HT sample (d, e), the P–HIP sample with the layer thickness 60 µm (f) and EDX analysis of the P–HIP sample (g, h).

The structure of the C–HT sample (see Fig. 8a) shows visible grain boundaries with higher porosity (cluster of inclusions) in comparison to the C–HIP sample depicted in Fig. 8b. However, the amount of these defects corresponded to the concentrations normally existing in the cast structure. Slight differences could be observed in the case of materials subjected to post-process operations. The HIP post-process reduced several impurities such as voids and pores and the structure exhibited a favourable structure with the extruded carbides within each single grain. Grain boundaries with excluded hard structures are clearly distinguishable in the images of the etched samples The specimens after HIP studied by Pippa [71], showed partial recrystallization and presented precipitates concentrated especially at the grain boundary. The recrystallization is mainly influenced by solution treatment temperature. For solution heat treatments at 1200 °C and higher, the melt pool and scanning path morphologies completely vanished [48]. However, without a more detailed local analysis of the particle's composition, it is not possible to precisely determine its chemical composition. Most likely they are secondary carbides of the M23C6 type formed by the reaction of less stable carbides of the MC type with particles within γ phase [72]. The primal carbides are distributed uniformly inside the matrix in all examined samples. In contrast, the P–HT and P–HIP samples featured a relatively homogenized microstructure, with elongational grains along the build direction and clear boundaries, as shown in Fig. 8c and d.

The SEM microstructure analysis was performed for all variants of post-process operations as well as for the 3D printed and casted samples, in order to investigate the distribution of phases and structures in the material. For the analysis of the casted material, the observations were performed on the C–HT and C–HIP samples. The analysis was carried out on the longitudinal cross-sections (parallel to the printing direction) of the 3D printed P–HT, and P–HIP samples with the Z orientation. A total of four samples were prepared for the microstructure scanning via SEM. The microstructures of the individual samples captured by SEM are summarized in Fig. 9. The primary carbides are equally distributed inside the γ matrix in all the examined samples. All samples (cast and 3D printed) showed a high degree of homogeneity with only a occasional occurrence of gas shrinkages. The original structure of lamellar-excluded γ phases with MC carbides (characterized by the yellow arrows) forming eutectic cells, caused by the rapid cooling of the material during the casting, was removed by the heat treatment of the samples consisted of solution annealing, where the internal structure of the material was homogenized. Subsequent aging affected the re-exclusion of the γ'phase into a more favourable strengthening intermetallic structure within the γ matrix (see Fig. 9a) [73]. In the casted material, the primal carbides were homogeneously distributed in the matrix. The HIP operation (see Fig. 9b) inflicted the change of the shape of the excluded carbides (from needle-like to a more equal shape) to the more favourable one. The microstructure of the P–HT sample is depicted in Fig. 9c, where the homogeneous distribution of the carbides was disturbed by the needle-like formations. These similar descriptions of the microstructures of 3D printed Inconel have already been presented by Siddiqui et al. [74]. The fine particles (chemical composition is shown in Fig. 9d and e) with sizes of less than 5 µm are assumed to be carbides resulting from the heat treatment, corresponding to the MC-type carbides detected by EDX. The dual-phase microstructural configuration of γ and γ' were observed, while cellular and columnar structures were not detected in the P–HIP and P–HT samples. The results observed in [75] indicated that the grains of the as-deposited samples in the building direction exhibited a very fine cellular dendritic structure with fine Laves phase, which completely disappeared after HIP. The small particles seen in Fig. 9f are likely precipitates excluded during the aging and their chemical composition obtained by EDX is characterized in Fig. 9g. The needle-like delta phases (chemical composition see Fig. 9h) were not fully solved during the heat treatment or by the HIP post-process. Moreover, these phases can affect mechanical properties due to the possible stress concentration at these particles.

The grains of the materials subjected to HIP treatments were analysed via EBSD. For both, scanning was performed in the axial region of the respective cross-sectional sample, as well as in the vicinity of its periphery in order to evaluate structure homogeneity. Fig. 10a and b show grains' orientations via orientation image maps (OIM), together with HAGBs and LAGBs depicted in black and green, respectively, for the axial and peripheral regions of the 3D printed and HIP-ed sample. The respective graphical depictions of grain size distributions (area-weighted fractions of equivalent circle diameters) are then depicted in Fig. 10c and d.

Fig. 10a and b documenting the grains' orientations show that the 3D printed P–HIP sample did not exhibit any significant texture, as the colouring of the individual grains was more or less random. Analyses of grain boundaries revealed that the structure contained almost 100 % of HAGBs, regardless of the examined location. Both these findings correlate with the hypothesis that the structure underwent successful recrystallization during HIP (this conclusion is also supported by the occurrence of numerous twins within the structures). As regards the grain size (Fig. 10c and d), the mean equivalent circle diameter did not differ to a greater extent (compare 15.7 µm acquired in the axial region to 17.1 µm acquired in the peripheral region). The maximum grain sizes were also comparable (122.9 µm and 127.2 µm in the axis and periphery, respectively). The 3D printed P–HIP sample thus exhibited sufficient homogeneity. Also, no pores were detected to be present within the structure during the analyses.
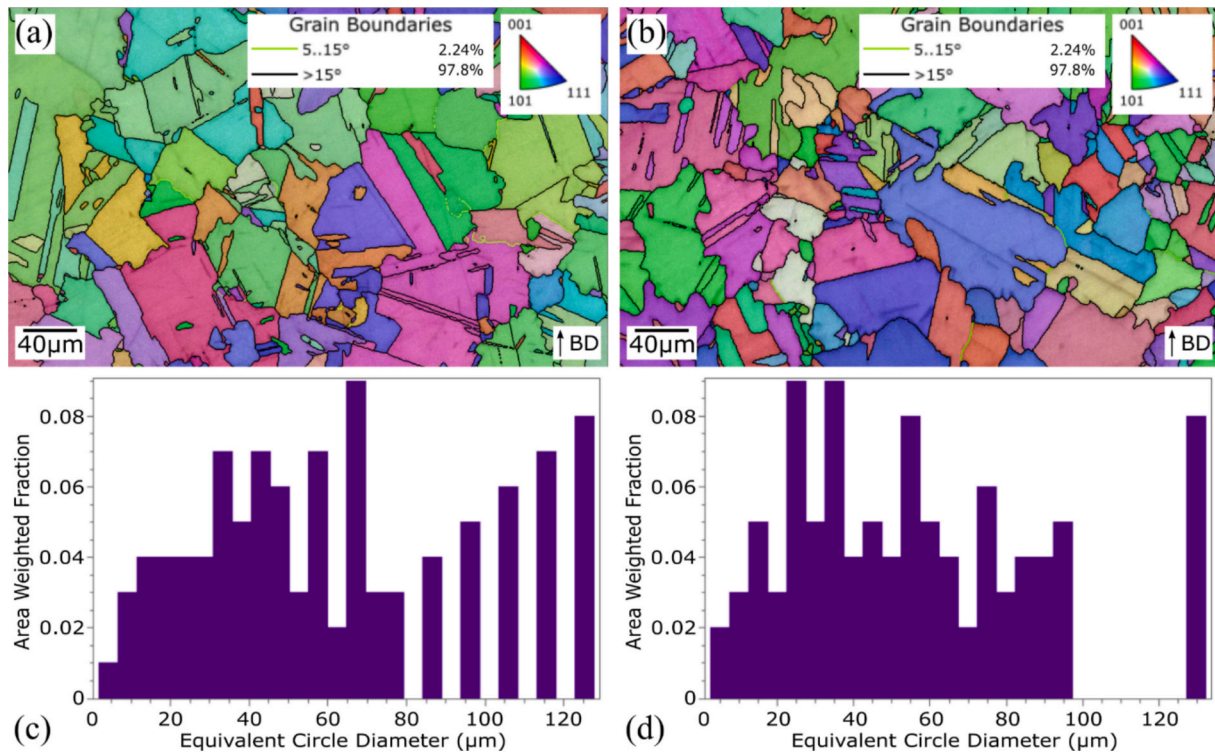
Fig. 10. OIM with HAGBs (black) and LAGBs (green) in axial (a) and peripheral (b) region of 3D-printed HIP-ed sample. Area-weighted fraction of equivalent circle diameter depicting grain size distribution in axial (c) and peripheral (d) region of the P–HIP sample. (For interpretation of the references to colour in this figure legend, the reader is referred to the web version of this article.)

OIMs with depicted HAGBs and LAGBs for the axial and peripheral regions of the C–HIP sample are shown in Fig. 11a and b, respectively, while the respective area-weighted fractions of equivalent circle diameters demonstrating grain size distributions are depicted in Fig. 11c and d.

The depicted scanned images evidently point to the fact that the grain size was incomparably larger than that acquired for the P–HIP sample; the scan of 2.5×2 mm was only able to acquire 15 and 21 grains (respectively for the axial and peripheral regions). By this reason, the conclusions drawn based on these scans are only informative.

The structures depicted in Fig. 11a and b show that the grains within the C–HIP sample had a tendency to preferably orient in $\langle 110 \rangle || z$ or $\langle 111 \rangle || z$ orientation. Also, some of the grains featured the development of subgrains – a fraction of LAGBs pointing to incomplete structure restoration was found in the axial region of the sample (Fig. 11a). No occurrence of LAGBs was found in the periphery of the sample. As regards the grain size, the acquired mean equivalent circle diameter was 440 μm in the axial region, and 398 in the peripheral region. Slightly larger grains were thus found in the vicinity of the axis (compared to the periphery). Nevertheless, as afore-stated, the grain count was not sufficient to provide reliable results. Neither the C–HIP sample exhibited any porosity within the structure.

The prepared lamellas were studied via TEM in order to distribute the individual chemical elements in the material. EDX measurements were performed on the P–HT and P–HIP samples. The lamella produced from the P–HT and P–HIP samples are shown in Fig. 12a and b, including the individual detail, in which the EDX analysis was performed. Based on the chemical analysis of the lamella from the P–HT sample, the MC and $M_{23}C_6$ carbides were identified in the γ matrix. The MC carbides (marked with the red arrows, based on the titanium and tantalum) are very stable and form just below the solidus temperature while the $M_{23}C_6$ (marked with the red circle, based on the chromium) originate during the heat treatment [76]. The MC carbides exhibited a dominantly needle-like shape, which can negatively affect mechanical properties.

Chemical analysis of the P–HIP sample showed none significant difference in the element distribution. Hence, it can be stated that the chemical composition of the individual elements is depicted also in Fig. 12, when the errors were considered, it turned out that both samples featured the similar concentration (the intervals overlapped). In contrast to the EDX measurement for the sample P–HT, the presence of chromium particles was not confirmed for the sample P–HIP. Considering the shape of the MC carbides a significant difference was observed after HIP post-process. Their shape changed from the needle-like to the more spherical shape, which promotes the mechanical properties.

3.6. Discussion

Inconel 939 is one of the materials used in constructions of turbochargers and gas turbine blades. Among the nickel superalloys processed by the PBF technology, Inconel 939 featured favourable material properties at the room temperature as well at the elevated temperature. The conventional processing of nickel superalloys is usually carried out by the precision casting technology in the combination with the subsequent machining. The standard process of prototyping using this technology involves long and cost development of technological process parameters and the subsequent time-consuming production. A possible way to accelerate and streamline production is the use of AM in the production process. Based on the obtained data the 3D printed Inconel 939 featured sufficient YS and UTS, which are required in the energy industry, especially in the impeller production. In comparison to the casted material the 3D printed one exhibited higher UTS, which is a crucial factor in the aforementioned applications. The HIP post-process brought a positive effect regarding the final porosity, average grain size, and high angle grain boundaries, which corresponded with the increased mechanical properties as well as with the creep resistance. The sample after the heat treatment and HIP underwent the full recrystallization and showed homogeneously distributed carbides with none observable pores and voids within the structure. TEM analysis showed a huge number of
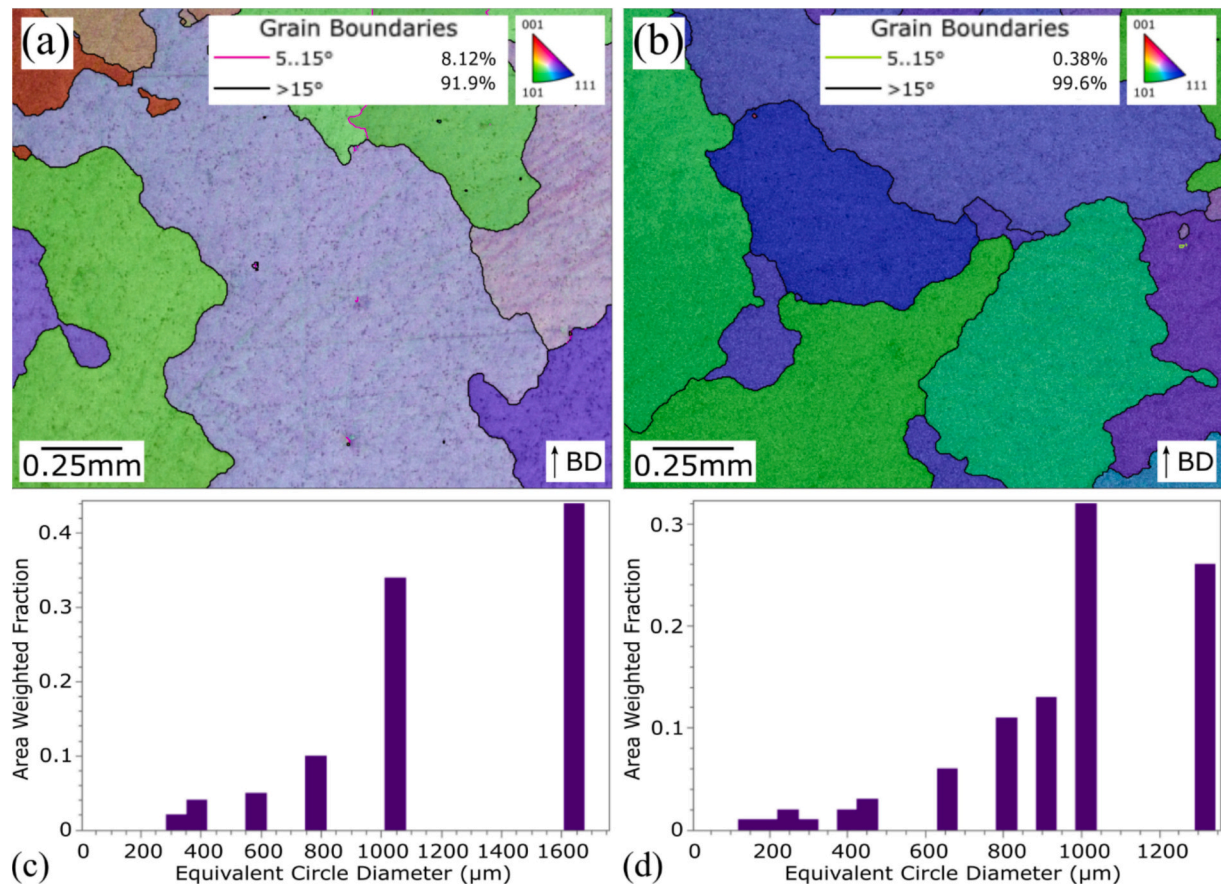
Fig. 11. OIM with HAGBs (black) and LAGBs (green) axial (a) and peripheral (b) region of the C–HIP sample. Area-weighted fraction of equivalent circle diameter depicting grain size distribution in axial (c) and peripheral (d) region of the C–HIP sample. (For interpretation of the references to colour in this figure legend, the reader is referred to the web version of this article.)
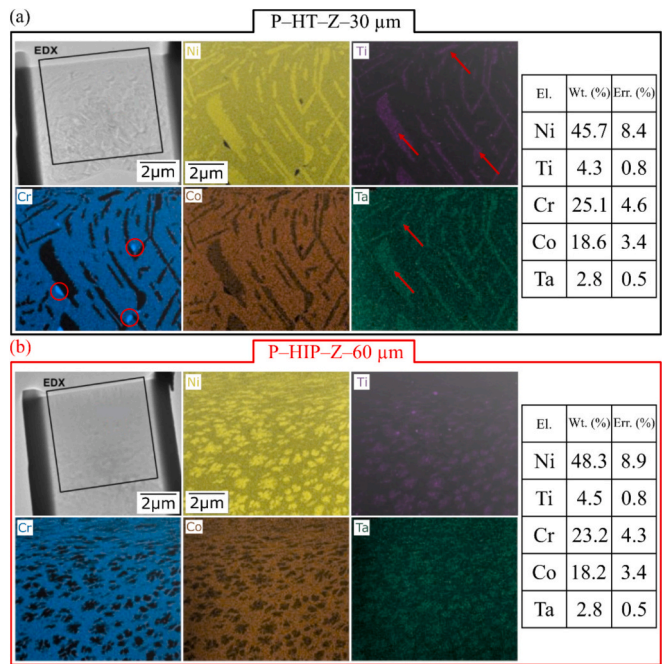
Fig. 12. TEM lamella including a map of the distribution of individual elements for the 3D printed sample P–HT (layer thickness 30 μm) (a) and the 3D printed sample P–HIP (layer thickness 60 μm).

nanoprecipitates equally spread within the 3D printed structure promoting the mechanical properties at the higher working temperature. If the PBF technology was involved in the impeller production, the delivery time of test prototypes to customers would be significantly reduced. Similarly, the development and the production capacity of the foundry would be released. The novelty of this study lies primarily in the possibility of using the AM technology in the production of a turbine engine axial impeller, which has not been published anywhere before. The 3D printed components do not often comply with surface quality requirements and the surface must be machined. The machinability of 3D printed material would be our next research.

4. Conclusion

In this study, the comparison of the 3D printed and cast material Inconel 939 intended for the production of the impeller of a turbine engine was performed in terms of mechanical properties (yield strength, ultimate tensile strength, creep resistance) and structure. The following conclusions were reached after many analyses and tests.

- The mechanical properties, especially the ultimate tensile strength and ductility increased after the HIP. Generally, HIP led to the improvement of the mechanical properties and structure changes.
- The results of the creep resistance of the 3D printed material showed a significantly higher creep resistance of the material with the layer thickness of 60 μm and post-processed by the HIP, but in the comparison to the casted samples they featured a lower creep resistance (break time and elongation) due to the lower average grain size.

- The 3D printed material showed a high degree of homogeneity compared to the casted material, with only occasional occurrence of gas shrinkages within the structure. The Ti and Ta carbides were monitored via EDX analysis, which exhibited an equal distribution within the subgrains.
- The EBSD analysis revealed that the 3D printed material featured a lower average grain size with almost 100 % high angle grain boundaries corresponding with the full recrystallization during the HIP, which entailed a lower creep resistance than the casted material.
- The TEM analysis of the lamella prepared from the 3D printed material with the layer thickness of 30 μm showed the existence of significant chromium particles within the structure, while after HIP they were not observed any longer, and the shape of the precipitates changed from the needle-like shape to more spheroidal one.

Based on the conclusions, it can be clearly stated that the Inconel 939 printed material, thanks to its satisfactory output from tensile tests, meets the requirements for its use, especially in heat-exposed applications. Hence Inconel 939 can be used as an effective substitution of the cast material variant in the aforementioned applications such as turbine engine axial impellers.

CRediT authorship contribution statement

Josef Sedlak: Conceptualization, Data curation, Formal analysis, Investigation, Methodology, Resources, Writing – original draft, Writing – review & editing. **Jan Zouhar:** Conceptualization, Data curation, Formal analysis, Methodology, Project administration, Validation, Writing – original draft, Writing – review & editing. **Zdenek Pokorny:** Conceptualization, Investigation, Methodology, Supervision, Validation, Writing – original draft, Writing – review & editing. **Jan Robl:** Conceptualization, Data curation, Funding acquisition, Investigation, Methodology, Writing – original draft, Writing – review & editing. **Stepan Kolomy:** Conceptualization, Data curation, Investigation, Methodology, Resources, Validation, Writing – original draft, Writing – review & editing. **Marek Pagac:** Conceptualization, Data curation, Formal analysis, Supervision, Validation, Writing – original draft, Writing – review & editing. **Karel Kouril:** Conceptualization, Data curation, Investigation, Methodology, Supervision, Writing – original draft, Writing – review & editing.

Declaration of competing interest

The authors declare that they have no known competing financial interests or personal relationships that could have appeared to influence the work reported in this paper.

Acknowledgments

References

[1] Gibson Ian, Rosen David WA, Stucker Brent. Additive manufacturing technologies. Boston: Springer-Verlag; 2010. https://doi.org/10.1007/978-1-4419-1120-9. ISBN 9781441911193.

[2] Kumar L Jyothish, Pandey Pulak Ma Wimpenny, Ian David. 3D printing and additive manufacturing technologies. Singapore: Springer Singapore Pte. Limited; 2018. https://doi.org/10.1007/978-981-13-0305-0. ISBN 9789811303043.

[3] Larimian Taban, Almangour Bandar, Grzesiak Dariusz, Walunj Ganesh A, Borkar Tushar. Effect of laser spot size, scanning strategy, scanning speed, and laser power on microstructure and mechanical behavior of 316L stainless steel fabricated via selective laser melting. J Mater Eng Perform 2021;31(3):2205–24. ISSN 1059–9495, https://doi.org/10.1007/s11665-021-06387-8 [cit. 2022-05-03].

[4] Pitrmuc Zdeněk, Šimota Jan, Beránek Libor, Mikeš Petr, Andronov Vladislav, et al. Mechanical and microstructural anisotropy of laser powder bed fusion 316L stainless steel. Materials 2022;15(2):551. ISSN 1996–1944, https://doi.org/10.3390/ma15020551 [cit. 2023-09-18].

[5] Nong XDA, Zhou XL. Effect of scanning strategy on the microstructure, texture, and mechanical properties of 15-5PH stainless steel processed by selective laser melting. Mater Charact 2021. https://doi.org/10.1016/j.matchar.2021.111012. 174, 111012. ISSN 1044–5803. Dostupné z. [cit. 2023-02-04].

[6] Kolomy Stepan, Jopek Miroslav, Sedlak Josef, Benc Marek A, Zouhar Jan. Study of dynamic behaviour via Taylor anvil test and structure observation of M300 maraging steel fabricated by the selective laser melting method. J Manuf Process 2024;125:283–94. ISSN 15266125, https://doi.org/10.1016/j.jmapro.2024.07.057 [cit. 2024-07-22].

[7] Gushchina Marina O, Kuzminova Yulia O, Kudryavtsev Egor A, Babkin Konstantin D, Andreeva Valentina D, et al. Effect of scanning strategy on mechanical properties of Ti-6Al-4V alloy manufactured by laser direct energy deposition. J Mater Eng Perform 2021;31(4):2783–91. ISSN 1059–9495. Dostupné z, https://doi.org/10.1007/s11665-021-06407-7 [cit. 2022-05-03].

[8] Kolomy Stepan, Sedlak Josef, Zouhar Jan, Slany Martin, Benc Marek, et al. Influence of aging temperature on mechanical properties and structure of M300 Maraging steel produced by selective laser melting. Materials 2023;16(3):977. ISSN 1996–1944. Dostupné z, https://doi.org/10.3390/ma16030977 [cit. 2023-01-29].

[9] Hajnys J, Pagac M, Mesicek J, Petru JA, Spalek F. Research of 316L metallic powder for use in SLM 3D printing. Adv Mater Sci 2020;20(1):5–15. ISSN 2083–4799, https://doi.org/10.2478/adms-2020-0001 [cit. 2024-03-29].

[10] Hajnys Jiri, Pagac Marek, Kotera Ondrej, Petru Jana A, Scholz Sebastian. Influence of basic process parameters on mechanical and internal properties of 316l steel in slm process for renishaw AM400. MM Science Journal 2019;01:2790–4. ISSN 18031269, 10.17973/MMSJ.2019_03_2018127 [cit. 2023-09-21].

[11] Dobrocky David, Pokorny Zdenek, Vitek Roman, Prochazka Jiri, Studeny Zbynek, et al. Possibilities of using the duplex system plasma Nitriding + CrN coating for special components. Coatings (Basel) 2022;12(12):1953. Dostupné z: https://doi.org/10.3390/coatings12121953 [cit. 2023-01-20].

[12] Opěla Petr, Benč Marek, Kolomy Stepan, Jakůbek Zdeněk A, Beranová Denisa. High cycle fatigue behaviour of 316L stainless steel produced via selective laser melting method and post processed by hot rotary swaging. Materials 2023;16(9):3400. ISSN 1996–1944, https://doi.org/10.3390/ma16093400 [cit. 2023-05-22].

[13] Xie Jilin, Ma Yingche, Xing Weiwei, Zhang Long, Ou Meiqiong, et al. Heat-affected zone crack healing in IN939 repaired joints using hot isostatic pressing. Welding in the World 2018;62(3):471–9. ISSN 0043–2288, https://doi.org/10.1007/s40194-018-0579-5 [cit. 2023-05-24].

[14] Pathak Sunil, Zulić Sanin, Kaufman Jan, Kopeček Jaromír, Stránský Ondřej, et al. Post-processing of selective laser melting manufactured SS-304L by laser shock peening. J Mater Res Technol 2022;19(2):4787–92. ISSN 22387854, https://doi.org/10.1016/j.jmrt.2022.07.014 [cit. 2023-09-18].

[15] Primus Tomáš, Beránek Libor, Pitrmuc Zdeněk, Šimota Jan A, Zeman Pavel. Laser polishing of additively manufactured 316L stainless steel with different construction angles. Int J Adv Manuf Technol 2022;121:5–6. 3215–3228. ISSN 0268–3768, https://doi.org/10.1007/s00170-022-09514-4 [cit. 2023-09-18].

[16] Mesicek Jakub, Jancar Lukas, MA Quoc-Phu, Hajnys Jiri, Tanski Tomasz, et al. Comprehensive view of topological optimization scooter frame design and manufacturing. Symmetry 2021;13(7). https://doi.org/10.3390/sym13071201. ISSN 2073–8994. [cit. 2023-09-21].

[17] Mesicek Jakub, Pagac Marek, Petru Jana, Novak Petr, Hajnys Jiri, et al. Topological optimization of the formula student bell crank. MM Science Journal 2019;2019(03):2964–8. ISSN 18031269, 10.17973/MMSJ.2019_10_201893 [cit. 2024-03-29].

[18] Sen Ceren, Subasi Levent, Ozaner Ozan Can A, Orhangul Akin. The effect of milling parameters on surface properties of additively manufactured Inconel 939. Procedia CIRP 2020;87:31–4. ISSN 2212–8271, https://doi.org/10.1016/j.procir.2020.02.072 [cit. 2023-05-24].

[19] Kolomy Stepan, Maly Martin, Sedlak Josef, Zouhar Jan, Slany Martin, et al. Machinability of extruded H13 tool steel: effect of cutting parameters on cutting forces, surface roughness, microstructure, and residual stresses. Alex Eng J 2024; 99:394–407. ISSN 1110–0168, https://doi.org/10.1016/j.aej.2024.05.018 [cit. 2024-07-17].

[20] Deirmina Faraz, Peghini Nicola, Almangour Bandar, Grzesiak Dariusz A, Pellizzari Massimo. Heat treatment and properties of a hot work tool steel fabricated by additive manufacturing. Materials Science & Engineering A, Structural Materials: Properties, Microstructure and Processing 2019;753:109–21. ISSN 0921–5093, https://doi.org/10.1016/j.msea.2019.03.027 [cit. 2023-02-05].

[21] Buschow KHJ. Encyclopedia of materials: Science and technologyvol. 2. C. Amsterdam, London: Elsevier; 2001 [ISBN 0–08–043152-6].

[22] Ozaner Ozan Can, Dursun Gokhan, a Akbulut, Guray.. Effects of wire-EDM parameters on the surface integrity and mechanical characteristics of additively manufactured Inconel 939. In: Materials today: Proceedings. Elsevier; 2021.

p. 1861–5. ISSN 2214–7853, https://doi.org/10.1016/j.matpr.2020.08.486 [cit. 2023-06-02].

[23] Blakey-Milner Byron, Gradl Paul, Snedden Glen, Brooks Michael, Pitot Jean, et al. Metal additive manufacturing in aerospace: a review. Mater Des 2021;209:110008. ISSN 0264–1275, https://doi.org/10.1016/j.matdes.2021.110008 [cit. 2023-05-23].

[24] Ezugwu EO, Bonney JA, Yamane Y. An overview of the machinability of aeroengine alloys. J Mater Process Technol 2003;134(2):233–53. ISSN 0924–0136, https://doi.org/10.1016/S0924-0136(02)01042-7 [cit. 2023-05-23].

[25] Anderson Roger, Viteri Fermin, Hollis Rebecca, Hebbar Mohan, Downs James, et al. Application of existing turbomachinery for zero emissions oxy-fuel power systemsvol. 1; 2010. p. 469–79. ISSN 978–0–7918-4882-1, https://doi.org/10.1115/GT2009-59995 [cit. 2023-05-23].

[26] Thellaputta Gopala Rao, Chandra Pulcharu Subhash A, RAO CSP. Machinability of nickel based superalloys: a review. Materials Today: Proceedings 2017;4(2): 3712–21. ISSN 2214–7853, https://doi.org/10.1016/j.matpr.2017.02.266 [cit. 2023-05-23].

[27] Kubickova Lea, Kormanakova Marcela, Vesela Lucie A, Jelinkova Zdenka. The implementation of industry 4.0 elements as a tool stimulating the competitiveness of engineering enterprises. Journal of Competitiveness 2021;13(1):76–94. ISSN 1804-171X, https://doi.org/10.7441/joc.2021.01.05 [cit. 2023-08-04].

[28] Yang Li, Baughman Brian, Godfrey Donald A, Hsu Keng. Additive manufacturing of metals: The technology, materials, design and production. Cham: Springer Nature; 2017. https://doi.org/10.1007/978-3-319-55128-9. ISBN 9783319551289. ISSN 1860–5168.

[29] Kanagarajah P, Brenne F, Niendorf TA, Maier HJ. Inconel 939 processed by selective laser melting: effect of microstructure and temperature on the mechanical properties under static and cyclic loading. Materials Science & Engineering A, Structural Materials: Properties, Microstructure and Processing 2013;588:188–95. ISSN 0921–5093, https://doi.org/10.1016/j.msea.2013.09.025 [cit. 2023-05-23].

[30] Banoth Santhosh, Li Chen-wei, Hiratsuka Yo A, Kakehi Koji. The effect of recrystallization on creep properties of alloy in939 fabricated by selective laser melting process. Metals (Basel) 2020;10(8):1–16. ISSN 2075–4701, https://doi.org/10.3390/met10081016 [cit. 2023-05-23].

[31] Sundararaman MA, Singh JB. Design considerations for a high temperature creep resistant nickel base alloy. Trans Indian Inst Metals 2010;63(2–3):313–9. ISSN 0972–2815, https://doi.org/10.1007/s12666-010-0042-9 [cit. 2023-05-23].

[32] Divya VD, Muñoz-Moreno R, Messé OMDM, Barnard JS, Baker S, et al. Microstructure of selective laser melted CM247LC nickel-based superalloy and its evolution through heat treatment. Mater Charact 2016;114:62–74. ISSN 1044–5803, https://doi.org/10.1016/j.matchar.2016.02.004 [cit. 2023-05-23].

[33] Mellin Pelle, Lyckfeldt Ola, Harlin Peter, Brodin Håkan, Blom Henrik, et al. Evaluating flowability of additive manufacturing powders, using the Gustavsson flow meter. Metal Powder Report 2017;72(5):322–6. ISSN 0026–0657, https://doi.org/10.1016/j.mprp.2017.06.003 [cit. 2023-05-23].

[34] Tang Yuanbo T, Panwisawas Chinnapat, Ghoussoub Joseph N, Gong Yilun, Clark John WG, et al. Alloys-by-design: application to new superalloys for additive manufacturing. Acta Mater 2021;202:417–36. ISSN 1359–6454, https://doi.org/10.1016/j.actamat.2020.09.023 [cit. 2024–12–31].

[35] Marchese Giulio, Parizia Simone, Saboori Abdollah, Manfredi Diego, Lombardi Mariangela, et al. The influence of the process parameters on the densification and microstructure development of laser powder bed fused inconel 939. Metals (Basel) 2020;10(7):1–19. ISSN 2075–4701, https://doi.org/10.3390/met10070882 [cit. 2023-05-24].

[36] Ozaner Ozan Can, Karabulut Şener A, Izciler Mahmut. Study of the surface integrity and mechanical properties of turbine blade fir trees manufactured in Inconel 939 using laser powder bed fusion. J Manuf Process 2022;79:47–59. ISSN 1526–6125, https://doi.org/10.1016/j.jmapro.2022.04.054 [cit. 2023-05-24].

[37] Raute J, Jokisch T, Biegler MA, Rethmeier M. Effects on crack formation of additive manufactured Inconel 939 sheets during electron beam welding. Vacuum 2022; 195:110649. ISSN 0042-207X, https://doi.org/10.1016/j.vacuum.2021.110649 [cit. 2023-05-24].

[38] González MA, Martínez DI, Pérez A, Guajardo HA, Garza A. Microstructural response to heat affected zone cracking of prewelding heat-treated Inconel 939 superalloy. Mater Charact 2011;62(12):1116–23. ISSN 1044–5803, https://doi.org/10.1016/j.matchar.2011.09.006 [cit. 2023-05-24].

[39] Moattari M, Shokrieh MMA, Moshayedi H. Effects of residual stresses induced by repair welding on the fracture toughness of Ni-based IN939 alloy. Theor Appl Fract Mech 2020;108:102614. ISSN 0167–8442, https://doi.org/10.1016/j.tafmec.2020.102614 [cit. 2023-05-24].

[40] González Albarrán MA, Martínez DI, Díaz E, Díaz JC, Guzman I, et al. Effect of preweld heat treatment on the microstructure of heat-affected zone (HAZ) and weldability of Inconel 939 superalloy. J Mater Eng Perform 2014;23(4):1125–30. ISSN 1059–9495, https://doi.org/10.1007/s11665-013-0704-y [cit. 2023-05-24].

[41] Kumar, Nandha E, Athira KS, Chatterjee Subhradeep A, Srinivasan Dheepa. Effect of heat treatment on structure and properties of laser powder bed fusion Inconel 939. International Additive Manufacturing Conference 2023. https://doi.org/10.1115/IAM2022-93945 [cit. 2024-12–31].

[42] Zhu Jingxi, Wise Adam, Nuhfer Thomas, Holcomb Gordon R, Jablonski Paul D, et al. High-temperature-oxidation-induced ordered structure in Inconel 939 superalloy exposed to oxy-combustion environments. Materials Science & Engineering A, Structural Materials: Properties, Microstructure and Processing 2013;566(C):134–42. ISSN 0921–5093, https://doi.org/10.1016/j.msea.2012.12.074 [cit. 2023-05-24].

[43] Miskovic Z, Jovanovic M, Gligic MA, Lukic B. Microstructural investigation of IN 939 superalloy. Online Vacuum 1991;43(5–7):709–11 [ISSN 0042-207X. [cit. 2023-05-24].

[44] Gusain, Rukesh, Dodaran, Mohammad Soleimani, Grad, Paul R., Shamsaei, Nima A Shao, Shuai. The influence of heat treatments on the microstructure and tensile properties of additively manufactured Inconel 939. In: Marshall space flight center. [cit. 2024–12–31].

[45] Jahangiri Mohammadreza. Different effects of γ' and η phases on the physical and mechanical properties of superalloys. J Alloys Compd 2019;802:535–45. ISSN 0925–8388, https://doi.org/10.1016/j.jallcom.2019.06.249 [cit. 2023-05-24].

[46] Jahangiri MR, Arabi HA, Boutorabi SMA. Comparison of microstructural stability of IN939 superalloy with two different manufacturing routes during long-time aging. Trans Nonferrous Metals Soc China 2014;24(6):1717–29. ISSN 1003–6326, https://doi.org/10.1016/S1003-6326(14)63245-3 [cit. 2023-05-24].

[47] Shaikh Abdul Shaafi, Rashidi Masoud, Minet-Lallemand Kevin A, Hryha Eduard. On as-built microstructure and necessity of solution treatment in additively manufactured Inconel 939. Powder Metall 2023;66(1):3–11. ISSN 0032–5899, https://doi.org/10.1080/00325899.2022.2041787 [cit. 2023-05-24].

[48] Doğu Merve Nur, Ozer Seren, Yalçin Mustafa Alp, Davut Kemal, Bilgin Güney Mert, et al. Effect of solution heat treatment on the microstructure and crystallographic texture of IN939 fabricated by powder bed fusion-laser beam. J Mater Res Technol 2023;24:8909–23. ISSN 2238–7854, https://doi.org/10.1016/j.jmrt.2023.05.152 [cit. 2024–12–31].

[49] Chang H, Lee C, Tang TPA, Ho HH. Evaluation of HIP pressure on Inconel 718 superalloy. International Journal of Cast Metals Research (Online) 2006;19(3): 181–7. ISSN 1364–0461, https://doi.org/10.1179/136404606225023408 [cit. 2023-05-30].

[50] Yao Yi, Wang Kaiwen, Wang Xiaoqing, Li Lin, Cai Wenjun, et al. Microstructural heterogeneity and mechanical anisotropy of 18Ni-330 maraging steel fabricated by selective laser melting: the effect of build orientation and height. J Mater Res 2020; 35(15):2065–76. ISSN 0884–2914, https://doi.org/10.1557/jmr.2020.126 [cit. 2022-04-28].

[51] Król Mariusz, Snopiński Przemysław, Hajnyš Jiří, Pagáč Marek A, Łukowiec Dariusz. Selective laser melting of 18Ni-300 maraging steel. Materials 2020;13(19):4268. ISSN 1996–1944, https://doi.org/10.3390/MA13194268 [cit. 2024-07-30].

[52] Pathak Sunil, Böhm Marek, Kaufman Jan, Kopeček Jaromír, Zulić Sanin, et al. Microstructure and surface quality of SLM printed miniature helical gear in LSPwC. Surf Eng 2023;39(2):229–37. ISSN 0267–0844, https://doi.org/10.1080/02670844.2023.2207934 [cit. 2023-09-18].

[53] Wang Pan, Huang Pengfei, Ng Fern Lan, Sin Wai Jack, Lu Shenglu, et al. Additively manufactured CoCrFeNiMn high-entropy alloy via pre-alloyed powder. Mater Des 2019;168:107576. ISSN 0264–1275, https://doi.org/10.1016/j.matdes.2018.107576 [cit. 2022–10–07].

[54] Wang Pan, Song Jie, Nai Mui Ling, Sharon A, Wei Jun. Experimental analysis of additively manufactured component and design guidelines for lightweight structures: a case study using electron beam melting. Addit Manuf 2020;33: 101088. ISSN 2214–8604, https://doi.org/10.1016/j.addma.2020.101088 [cit. 2022–10–07].

[55] Kaynak Yusuf A, Kitay Ozhan. Porosity, surface quality, microhardness and microstructure of selective laser melted 316l stainless steel resulting from finish machining. Journal of Manufacturing and Materials Processing 2018;2(2):36. ISSN 2504–4494, https://doi.org/10.3390/jmmp2020036 [cit. 2022-12-06].

[56] Andronov Vladislav, Šimota Jan, Beránek Libor, Blažek Jiří A, Rušar Filip. Optimization of process parameters for additively produced tool steel 1.2709 with a layer thickness of 100 μm. Materials 2021;14(11):2852. ISSN 1996–1944, https://doi.org/10.3390/ma14112852 [cit. 2024-08-26].

[57] Nguyen QB, Zhu Z, Chua BW, Zhou W, Wei J, et al. Development of WC-Inconel composites using selective laser melting. Archives of Civil and Mechanical Engineering 2018;18(4):1410–20. ISSN 1644–9665, https://doi.org/10.1016/j.acme.2018.05.001 [cit. 2023-06-02].

[58] Nguyen Quy Bau, Nai Mui Ling, Sharon Zhu, Zhiguang Sun, Chen-nan Wei, Jun, et al. Characteristics of Inconel powders for powder-bed additive manufacturing. Engineering (Beijing, China) 2017;3(5):695–700. ISSN 2095–8099, https://doi.org/10.1016/J.ENG.2017.05.012 [cit. 2023-06-02].

[59] Chang Shih-hsien. In situ TEM observation of γ', γ'' and δ precipitations on Inconel 718 superalloy through HIP treatment. J Alloys Compd 2009;486(1):716–21. ISSN 0925–8388, https://doi.org/10.1016/j.jallcom.2009.07.046 [cit. 2023-06-06].

[60] Shingledecker, J.P., Evans, N.D. A Pharr, G.M. Influences of composition and grain size on creep-rupture behavior of Inconel alloy 740. 277–286 doi:https://doi.org/10.1016/j.msea.2013.04.087. [cit. 2023-06-06].

[61] Moussaoui K, Rubio W, Mousseigne M, Sultan TA, Rezai F. Effects of selective laser melting additive manufacturing parameters of Inconel 718 on porosity, microstructure and mechanical properties. Materials Science & Engineering A, Structural Materials: Properties, Microstructure and Processing 2018;735:182–90. ISSN 0921–5093, https://doi.org/10.1016/j.msea.2018.08.037 [cit. 2023-06-06].

[62] Lee Yo Seob, Kim Dae Whan, Lee Dok Yol A, Ryu Woo Seog. Effect of grain size on creep properties of type 316LN stainless steel. Met Mater Int 2001;7(2):107–14. ISSN 1598–9623, https://doi.org/10.1007/BF03026948 [cit. 2023-06-06].

[63] Popovich VA, Borisov EV, Heurtebise V, Riemslag T, Popovich AA, et al. Creep and thermomechanical fatigue of functionally graded Inconel 718 produced by additive manufacturing. 2018. p. 85–97. ISBN 978–3–319-72525-3, https://doi.org/10.1007/978-3-319-72526-0_9 [cit. 2023-06-06].

[64] Shi JJ, Li X, Zhang ZX, Cao GH, Russell AM, et al. Study on the microstructure and creep behavior of Inconel 718 superalloy fabricated by selective laser melting. Materials Science & Engineering A, Structural Materials: Properties, Microstructure

and Processing 2019;765:138282. ISSN 0921–5093, https://doi.org/10.1016/j.msea.2019.138282 [cit. 2023-06-06].

[65] Shi JJ, Zhou SA, Chen HH, Cao GH, Russell AM, et al. Microstructure and creep anisotropy of Inconel 718 alloy processed by selective laser melting. Materials Science & Engineering A, Structural Materials: Properties, Microstructure and Processing 2021;805:140583. ISSN 0921–5093, https://doi.org/10.1016/j.msea.2020.140583 [cit. 2024–12–31].

[66] Leary Martin, Mazur Maciej, Williams Hugh, Yang Eric, Alghamdi Ahmad, et al. Inconel 625 lattice structures manufactured by selective laser melting (SLM): mechanical properties, deformation and failure modes. Mater Des 2018;157: 179–99. ISSN 0264–1275, https://doi.org/10.1016/j.matdes.2018.06.010 [cit. 2023-06-06].

[67] Nguyen QB, Luu DN, Nai ML, Zhu Z, Chen Z, et al. The role of powder layer thickness on the quality of SLM printed parts. Archives of Civil and Mechanical Engineering 2018;18(3):948–55. ISSN 1644–9665, https://doi.org/10.1016/j.acme.2018.01.015 [cit. 2023-07-18].

[68] Pradeep PI, Kumar, Anil V, Venkateswaran T, Aswin S, Nair Vishnu, et al. Processing and characterization of 3D-printed Inconel-718 component through laser powder bed fusion route for high-temperature space application. Transactions of the Indian National Academy of Engineering (Online) 2021;6(1):133–46. ISSN 2662–5415, https://doi.org/10.1007/s41403-020-00196-6 [cit. 2023-07-18].

[69] Mclouth Tait D, Witkin David B, Lohser Julian R, Bean Glenn E, Sitzman Scott D, et al. Elevated temperature notch sensitivity of Inconel 718 manufactured by selective laser melting. J Mater Eng Perform 2021;30(7):4882–90. ISSN 1059–9495, https://doi.org/10.1007/s11665-021-05522-9 [cit. 2023-07-18].

[70] Wang Yachao, Shi Jing, Lu Shiqiang A, Wang Yun. Selective laser melting of graphene-reinforced Inconel 718 superalloy: evaluation of microstructure and tensile performance. J Manuf Sci Eng 2017;139:4. ISSN 1087–1357, https://doi.org/10.1115/1.4034712 [cit. 2023-07-18].

[71] Pippa Martina. Study of post-process treatments applied on the Inconel 939 superalloy produced by laser powder bed fusion. Torino. https://webthesis.biblio.polito.it/18373/; 2021 [cit. 2024–12–31].

[72] Zhou Wenzhe, Tian Yusheng, Wei Dongyu, Tan Qingbiao, Kong Decheng, et al. Effects of heat treatments on the microstructure and tensile properties of IN738 superalloy with high carbon content fabricated via laser powder bed fusion. J Alloys Compd 2023;953:170110. ISSN 0925–8388, https://doi.org/10.1016/j.jallcom.2023.170110 [cit. 2023-07-10].

[73] Murali Aashish. Phase and residual stress analysis of alloys 600/82 used in nuclear reactor components. 2016. https://doi.org/10.13140/RG.2.2.21603.55842 [cit. 2024–12–31].

[74] Siddiqui Sanna F, Fasoro Abiodun AA, Gordon Ali P. Selective laser melting (SLM) of Ni-based superalloys. In: Additive manufacturing handbook. CRC Press; 2017. p. 225–45. ISBN 9781482264081, https://doi.org/10.1201/9781315119106-14.

[75] Shi Lei, Lei Li-Ming, Wang Wei, Fu Xin A, Zhang Guang-ping. Effects of hot isostatic pressing and heat treatment process on microstructure and tensile properties of selective laser melting manufactured GH4169 alloy. Cai Liao Gong Cheng = Journal of Materials Engineering 2020;48(6):148–55. ISSN 1001–4381, 10.11868/j.issn.1001-4381.2019.000416 [cit. 2024–12–31].

[76] Smith William F. Structure and properties of engineering alloys. 2nd ed. New York: McGraw-Hill; 1993 [ISBN 0–07–112829-8].